



Discovery of a [C I]-faint, CO-bright Galaxy: ALMA Observations of the Merging Galaxy NGC 6052

Tomonari Michiyama¹ , Junko Ueda² , Ken-ichi Tadaki² , Alberto Bolatto³ , Juan Molina¹, Toshiki Saito⁴ , Takuji Yamashita^{2,5} , Ming-Yang Zhuang^{1,6} , Kouichiro Nakanishi^{2,7} , Daisuke Iono^{2,7} , Ran Wang^{1,6} , and Luis C. Ho^{1,6}

¹ Kavli Institute for Astronomy and Astrophysics, Peking University, 5 Yiheyuan Road, Haidian District, Beijing 100871, People's Republic of China
t.michiyama.astr@gmail.com

² National Astronomical Observatory of Japan, National Institutes of Natural Sciences, 2-21-1 Osawa, Mitaka, Tokyo, 181-8588, Japan

³ Department of Astronomy and Laboratory for Millimeter-Wave Astronomy, University of Maryland, College Park, MD 20742, USA

⁴ Max-Planck-Institut für Astronomie, Königstuhl 17, D-69117 Heidelberg, Germany

⁵ Research Center for Space and Cosmic Evolution, Ehime University, 2-5 Bunkyo-cho, Matsuyama, Ehime 790-8577, Japan

⁶ Department of Astronomy, School of Physics, Peking University, Beijing 100871, People's Republic of China

⁷ Department of Astronomical Science, The Graduate University for Advanced Studies, SOKENDAI, 2-21-1 Osawa, Mitaka, Tokyo 181-8588, Japan

Received 2020 April 15; revised 2020 June 11; accepted 2020 June 16; published 2020 July 6

Abstract

We report sensitive [C I] $^3P_1-^3P_0$ and $^{12}\text{CO } J=4-3$ observations of the nearby merging galaxy NGC 6052 using the Morita (Atacama Compact) Array of the Atacama Large Millimeter/submillimeter Array (ALMA). We detect $^{12}\text{CO } J=4-3$ toward the northern part of NGC 6052, but [C I] $^3P_1-^3P_0$ is not detected with a [C I] $^3P_1-^3P_0$ to $^{12}\text{CO } J=4-3$ line luminosity ratio of $\lesssim 0.07$. According to models of photodissociation regions, the unusual weakness of [C I] $^3P_1-^3P_0$ relative to $^{12}\text{CO } J=4-3$ can be explained if the interstellar medium has a hydrogen density larger than 10^5 cm^{-3} , conditions that might arise naturally in the ongoing merging process in NGC 6052. Its [C I] $^3P_1-^3P_0$ emission is also weaker than expected given the molecular gas mass inferred from previous measurements of $^{12}\text{CO } J=1-0$ and $^{12}\text{CO } J=2-1$. This suggests that [C I] $^3P_1-^3P_0$ may not be a reliable tracer of molecular gas mass in this galaxy. NGC 6052 is a unique laboratory to investigate how the merger process impacts the molecular gas distribution.

Unified Astronomy Thesaurus concepts: [Galaxy evolution \(594\)](#); [Galaxy interactions \(600\)](#); [Interstellar medium \(847\)](#); [Submillimeter astronomy \(1647\)](#)

1. Introduction

The atomic carbon emission line with the lower forbidden 3P fine structure ([C I] $^3P_1-^3P_0$, hereafter [C I] (1–0)) has a frequency of 492 GHz ($\lambda \simeq 609 \mu\text{m}$). In the classical framework of photodissociation region (PDR) theory (e.g., Tielens & Hollenbach 1985), the ultraviolet (UV) photons from young massive stars control the properties of the interstellar medium (ISM) and [C I] emission mostly arises from a narrow transition layer between [C II] and CO. On the other hand, [C I] observations for Galactic molecular clouds (0.1–1 pc scales) frequently show spatial coincidence between [C I] and CO emission lines and brightness temperatures very similar to that of $^{13}\text{CO } J=1-0$ (e.g., Ojha et al. 2001; Oka et al. 2001; Ikeda et al. 2002; Kramer et al. 2008; Shimajiri et al. 2013; Burton et al. 2015). This suggests that [C I] emission can be used to trace the bulk molecular gas mass in clouds. Papadopoulos et al. (2004) proposed the ubiquitous distribution of atomic carbon throughout a typical Giant Molecular Cloud is due to the combination of dynamics and the nonequilibrium chemistry processes, and Papadopoulos & Greve (2004) showed agreement between molecular gas masses estimated from [C I] and ^{12}CO emission lines in Arp 220 and NGC 6240.

An increasing number of [C I] emission line observations of extragalactic sources have been reported. The Spectral and Photometric Imaging Receiver Fourier Transform Spectrometer (SPIRE/FTS) mounted on the Hershel Space Observatory measured [C I] luminosities for ultra/luminous infrared galaxies (U/LIRGs) (Kamenetzky et al. 2016; Lu et al. 2017). The operation of high-frequency receivers (e.g., Bands 8 and 10 receivers) on the Atacama Large Millimeter/submillimeter Array

(ALMA) has also enabled investigations of the ~ 10 pc resolution distribution of atomic carbon in the nucleus (< 1 kpc) of nearby galaxies (e.g., Krips et al. 2016; Izumi et al. 2020; Miyamoto et al. 2018; Salak et al. 2019) and ~ 100 pc scale maps of U/LIRGs such as NGC 6240 (Cicone et al. 2018) and IRAS F18293-3413 (T. Saito et al. 2020, in preparation). In addition, there is increasing availability of [C I] measurements of bright high- z galaxies, such as gravitational lensing galaxies and submillimeter galaxies (SMGs), that have been conducted using millimeter/submillimeter interferometers (e.g., Walter et al. 2011; Bothwell et al. 2017; Tadaki et al. 2018; Valentino et al. 2018, 2020).

The relation between [C I] and CO has been investigated using these data. Jiao et al. (2017, 2019) show a typical integrated brightness temperature ratio (i.e., units in $(\text{K km s}^{-1} \text{ pc}^2)$) of [C I] (1–0)/CO (1–0) ~ 0.2 and possible enhancement of [C I] abundance in U/LIRGs with respect to normal star-forming galaxies. Salak et al. (2019) find variations of the [C I] (1–0)/CO (1–0) ratio in 30–50 pc resolution data in the starburst galaxy NGC 1808, suggesting it is due to different excitation conditions and/or carbon abundance in different regions. Valentino et al. (2018, 2020) show a line luminosity ratio of [C I] (1–0)/CO (4–3) $\sim 0.1-3$ (in units of L_{\odot}) in $z \sim 1-2$ main sequence galaxies, suggesting this is driven by changes of the density in the range $n \sim 10^3-10^5 \text{ (cm}^{-3}\text{)}$ based on a simple PDR model (see also Bothwell et al. 2017).

The determination of the conversion factor from [C I] luminosity to molecular gas mass is a current research topic (Israel et al. 2015; Crocker et al. 2019; Heintz & Watson 2020). Recent theoretical models posit that atomic carbon is well mixed with H_2 in several environments, such as metal-poor

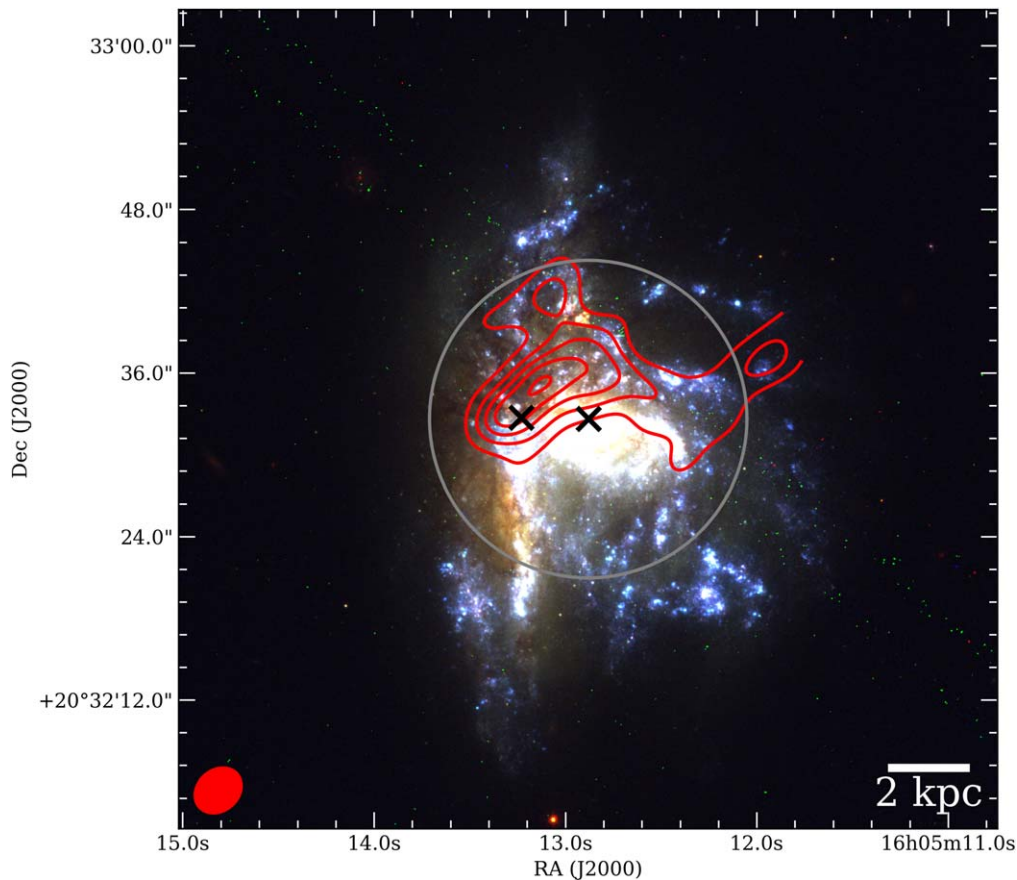


Figure 1. Three-color composite image of NGC 6052 from HST observations using the WFC3-F814W/F555W/F336W filters. The red contours show the CO (4–3) spatial distribution obtained from the Morita Array observation at 3, 6, 9, 12, and 15 σ levels with an achieved rms of 3.6 Jy km s⁻¹ beam⁻¹. The gray circle shows the FoV (FWHM of the primary beam $\sim 23''$) at the CO (4–3) sky frequency). The west and east nuclei are shown as X symbols. The pointing center is indicated by the western black X symbol (16^h05^m12^s.88, +20°32′32″.61 in ICRS frame). The positions of the western and eastern nuclei are based on NED. The synthesized beam (3″.8 \times 3″.1) and the spatial scale are shown at the bottom left and bottom right corners, respectively.

and/or sources with high cosmic-ray fluxes (e.g., Bisbas et al. 2015; Papadopoulos et al. 2018). In such environments [C I]-rich/CO-poor gas may be very abundant, suggesting that [C I] could be better than CO as a molecular gas mass tracer.

Summarizing the previous work, [C I] emission is expected to be an indicator of the cold molecular gas but its strength may depend on various parameters. To investigate it further it is necessary to collect a wider range of observations. The Morita Array (the official name of the Atacama Compact Array of 7 m diameter dishes) of ALMA enables us to investigate nearby galaxies with [C I] fluxes that were too low to be detectable with SPIRE/FTS. In this Letter, we report the nondetection of [C I] (1–0) and the detection of CO (4–3) in NGC 6052 using the Morita Array.

2. NGC 6052

NGC 6052 (Arp 209, UGC 10182, VV 86, Mrk 297) is a system of two colliding galaxies (east and west components) at a redshift of $z = 0.01581$ ⁸ (the corresponding luminosity distance is $D_L = 70.8$ Mpc, and the scale is $1'' \sim 333$ pc).⁹ The systemic velocity of $V_{\text{sys}} = 4666$ km s⁻¹ is calculated based on the radio velocity convention. The background of

Figure 1 is a three-color composite image of NGC 6052 obtained by the Wide Field Camera 3 (WFC3) on board the NASA/ESA Hubble Space Telescope.¹⁰ The positions of the west and east nuclei are shown by X symbols. Modeling by N -body simulations suggests that the evolutionary phase of this colliding system is about ~ 150 Myr after the first impact (Taniguchi & Noguchi 1991). The total infrared luminosity (8–1000 μm , L_{TIR}) of NGC 6052 is $\sim 10^{11.0} L_{\odot}$ based on Infrared Astronomical Satellite (IRAS) photometry (Sanders et al. 2003), which corresponds to a star formation rate (SFR) of $\text{SFR} \sim 18 M_{\odot} \text{yr}^{-1}$ using the calibration by Mo et al. (2010). The metallicity of NGC 6052 has been calculated in literature, but the values vary depending on the method: e.g., $12 + \log([\text{O}]/[\text{H}]) = 8.85$ (Sage et al. 1993) 8.65 (James et al. 2002), 8.34 (Shi et al. 2005), and 8.22–8.80 (Rupke et al. 2008). For the sake of simplicity, we assume the Milky Way metallicity for PDR modeling in Section 4.1.

3. Morita Array Observation

As a part of our ALMA Cycle 6 project (2018.1.00994.S), we carried out observations of NGC 6052 for [C I] (1–0) and CO (4–3) using a single pointing on 2019 April 21 and June 3, respectively. The pointing center is the west nucleus and the

⁸ Based on NASA/IPAC Extragalactic Database (NED).

⁹ Using the cosmology by Planck Collaboration Paper XIII, $H_0 = 67.7$ and $\Omega_m = 0.307$ (Planck Collaboration et al. 2016).

¹⁰ The WFC3 data were obtained from Hubble legacy archive (<https://hla.stsci.edu/hlview.html>) with the data set name of "hst_14066_05_wfc3_uvis_f814w_f555w_f336w."

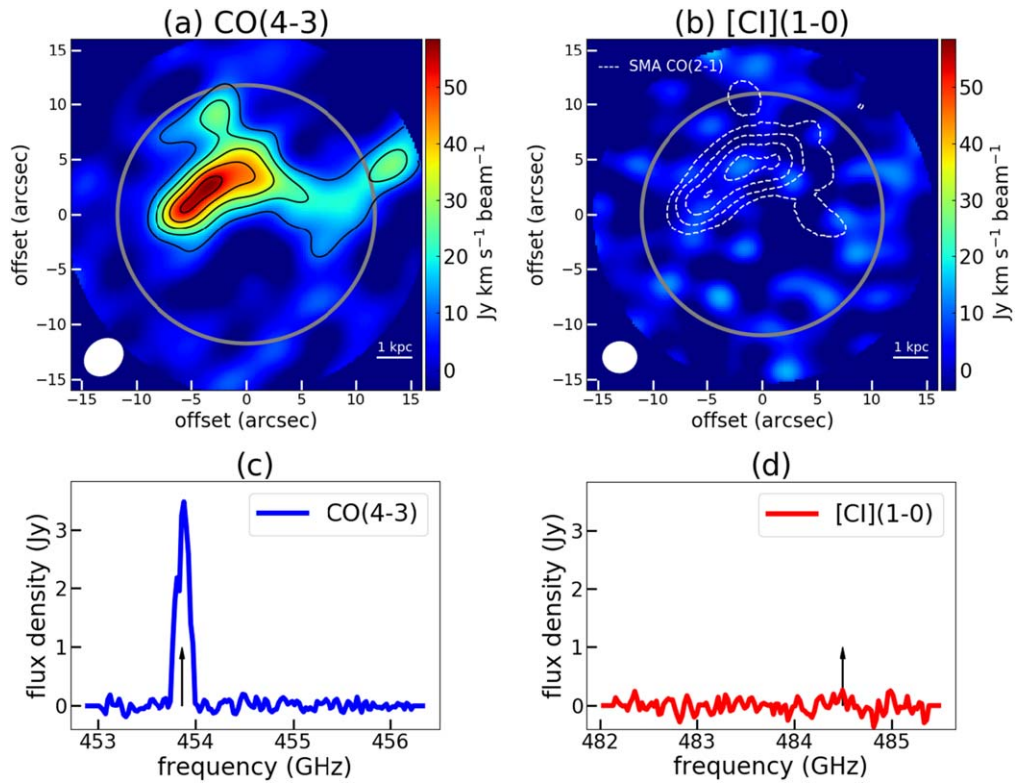


Figure 2. (top) Velocity-integrated intensity maps of the (a) CO (4–3) and (b) [C I] (1–0) emission lines. These were created by integrating the data cubes within the $[-72, 63]$ km s^{-1} velocity range (the systemic velocity is 4666 km s^{-1}) before applying the primary beam correction. In the CO (4–3) integrated intensity map, the black contours represent the same signal-to-noise levels as in Figure 1. In the [C I] (1–0) map, the synthesized beam size is $3''.1 \times 2''.8$ and the achieved rms level is $5.6 \text{ Jy km s}^{-1} \text{ beam}^{-1}$. The synthesized beam and the spatial scale are shown at the bottom left and bottom right corners, respectively. The white dashed lines show the CO (2–1) distribution obtained by SMA with the contour levels of (1.7, 8.5, 15.3, 22.1) $\text{Jy km s}^{-1} \text{ beam}^{-1}$ (Ueda et al. 2014). (bottom) Spectra integrated over the primary beam area. The velocity resolution is 15 km s^{-1} in both spectra. The rms of the spectra is 0.07 Jy and 0.1 Jy for (c) and (d), respectively. The black arrows indicate the frequencies of the CO (4–3) and [C I] (1–0) corresponding to the systemic velocity.

Table 1
Morita Array Observation Summary for NGC 6052

Line	Frequency (Rest/Sky) (GHz)	Synthesized Beam Size (arcsec)	rms (mJy beam^{-1})	Velocity Range (km s^{-1})	FWHM (km s^{-1})
(1)	(2)	(3)	(4)	(5)	(6)
[C I] (1–0)	492.16/484.50	$3''.1 \times 2''.8$	61.5	$[-72, 63]$...
CO (4–3)	461.04/453.86	$3''.8 \times 3''.1$	46.8	$[-72, 63]$	96

Note. (1) Line name. (2) The rest-frame and sky frequencies of the emission lines. (3) Synthesized beam size. (4) The rms level of the data cube with the velocity resolution of 15 km s^{-1} . (5) The velocity range for the velocity-integrated intensity map. The values are the relative velocity with respect to the systematic velocity of 4666 km s^{-1} . (6) The FWHM of the emission line.

half-power field of view (FoV) diameter is $23''.5$ at the frequency of CO (4–3) (Figure 1), with a maximum recoverable scale (MRS) of $13''.9$ ($\sim 4.6 \text{ kpc}$ for NGC 6052). The corresponding figures for [C I] (1–0) are 7% smaller. The calibrated visibility data were obtained by running the provided calibration scripts using CASA (version: 5.4.0-70; McMullin et al. 2007). The imaging was performed using `tclean` in CASA with a velocity resolution of 15 km s^{-1} , cell size of $0''.2$, image size of 200 pixels, and Briggs weighting with a robust parameter of 0.5. The clean masks for each channel were determined manually. The synthesized beam size and sensitivity at the velocity resolution of 15 km s^{-1} are shown in columns (3) and (4) of Table 1, respectively.

The intensity map integrated within the velocity range of $[-72, 63] \text{ km s}^{-1}$ is presented in Figure 2. The CO (4–3)

emission line is detected in the northern part of the galaxy, and it is offset from the optical peak. The CO (4–3) distribution is similar to CO (2–1) obtained by the Submillimeter Array (SMA; Ueda et al. 2014; Figure 2(b), white dashed contour). [C I] (1–0) emission is not detected within the FoV, particularly it is undetected in the region detected on the CO (4–3) and CO (2–1) peaks. We measure a velocity-integrated CO (4–3) flux of $S_{\text{CO}(4-3)} \Delta v = 414 \pm 124 \text{ Jy km s}^{-1}$ by integrating the spectrum over the entire FoV after correcting for the primary beam response (Figure 2(c), the velocity range is shown in Table 1). In this Letter, we adopt 30% as a conservative systematic uncertainty error, but this is not critical for our conclusions. We note that the error can be estimated from the rms level of the channel map (7 Jy km s^{-1}) with a systematic uncertainty associated with the expected absolute flux accuracy

Table 2
Line Properties of NGC 6052

Line	$S_{\text{line}}d\nu$ (Jy km s ⁻¹)	L'_{line} (K km s ⁻¹ pc ²)	L_{line} (L_{\odot})	Telescope	References
(1)	(2)	(3)	(4)	(5)	(6)
[C I] (1–0)	<28	<2 × 10 ⁷	<7 × 10 ⁴	Morita Array	this work
CO (1–0)	82	9.8 × 10 ⁸	4.7 × 10 ⁴	IRAM 30 m	Albrecht et al. (2007)
CO (2–1)	162 ± 32	(4.9 ± 1.0) × 10 ⁸	(1.9 ± 0.4) × 10 ⁵	SMA	Ueda et al. (2014)
CO (4–3)	414 ± 124	(3.1 ± 0.9) × 10 ⁸	(9.8 ± 2.9) × 10 ⁵	Morita Array	this work

Note. (1) Line name. (2) The velocity-integrated flux. We use the Jy to K conversion of 4.95 to derive the $S_{\text{line}}d\nu$ of CO (1–0) from the integrated intensity reported as 16.4 (K km s⁻¹) in the 24'' single-dish beam. (3) and (4) The line luminosity calculated by Equations (2) and (3). (5) The telescope name. (6) The reference literature for the line properties.

of 10% for ALMA Band 8.¹¹ However, the actual performance of the flux calibration has not been explored for the ACA standalone mode in Band 8 by the ALMA observatory.

We obtain a 3σ upper limit for the [C I] (1–0) velocity-integrated intensity using

$$S_{\text{line}}d\nu < 3\sigma_{\text{ch}}D_v \sqrt{\frac{N_{\text{ch}}N_{\text{box}}}{N_{\text{beam}}}} \\ = 28 \text{ Jy km s}^{-1}, \quad (1)$$

where $\sigma_{\text{ch}} = 61.5$ (mJy beam⁻¹) is the rms level of the channel map (Table 1), $D_v = 15$ km s⁻¹ is the velocity resolution, $N_{\text{ch}} = \text{FWHM}/D_v$, $\text{FWHM} = 96$ (km s⁻¹) assuming the same value with CO (4–3) line shape (Figure 2(c)), $N_{\text{box}} = 3990$ (the number of pixel where CO (4–3) is detected inside the 3σ contour of Figure 2(b)), $N_{\text{beam}} = 247$ is the number of pixel for the synthesized beam, following the equation from Hainline et al. (2004).

The velocity-integrated line fluxes and line luminosities including CO (1–0) and CO(2–1) values from the literature (Albrecht et al. 2007; Ueda et al. 2014) are summarized in Table 2. The luminosities for the lines are measured using

$$L_{\text{line}} (L_{\odot}) \\ = 1.04 \times 10^{-3} S_{\text{line}} \Delta\nu \nu_{\text{rest}} (1+z)^{-1} D_L^2 \quad (2)$$

and

$$L'_{\text{line}} (\text{K km s}^{-1} \text{ pc}^2) \\ = 3.25 \times 10^7 S_{\text{line}} \Delta\nu \nu_{\text{obs}}^{-2} (1+z)^{-3} D_L^2, \quad (3)$$

where $S_{\text{line}}\Delta\nu$ is the velocity-integrated flux in Jy km s⁻¹, ν_{rest} is the rest frequency of the observing line emission in GHz, z is the redshift, D_L is the luminosity distance in Mpc, and $\nu_{\text{obs}} = \nu_{\text{rest}}/(1+z)$ is the sky frequency for the observing line emission in GHz (Solomon & Vanden Bout 2005). We use L'_{line} to investigate the molecular gas mass (Section 4.2) and L_{line} to investigate the luminosity ratios for a PDR modeling (Section 4.1).

4. Discussion

4.1. Photodissociation Regions

In this section, we explain low $L_{[\text{C I}]}(1-0)/L_{\text{CO}(4-3)}$ of <0.07, which is not well documented in previous observations such as

¹¹ <https://almascience.nao.ac.jp/documents-and-tools/cycle6/alma-proposers-guide>

Israel & Baas (2002) and Valentino et al. (2020). We use the Photodissociation Region Toolbox (PDRT¹²; Kaufman et al. 1999, 2006; Pound & Wolfire 2008) to investigate density (n_{H}) and incident FUV radiation field (U_{uv} corresponding to photons with $6 \text{ eV} \leq h\nu < 13.6 \text{ eV}$) in units of the average interstellar radiation field in the vicinity of the Sun ($G_0 = 1.6 \times 10^{-3} \text{ ergs cm}^{-2} \text{ s}^{-1}$; Habing 1968). The modeling predicts line intensities for combinations of n_{H} and U_{uv} by self-consistently solving for chemical processes, radiation transfer, and thermal balance. Figure 3(a) shows the predictions for $L_{[\text{C I}]}(1-0)/L_{\text{CO}(4-3)}$ versus $L_{[\text{C I}]}(1-0)/L_{\text{TIR}}$ together with the data for nearby U/LIRGs observed by SPIRE/FTS (Kamenetzky et al. 2016), and the upper limits we obtain for NGC 6052. The red solid and blue dashed lines indicate the tracks for constant n_{H} and U_{uv} , respectively. According to the plane-parallel PDR model, the UV radiation cannot penetrate deeply into the molecular medium if the region is dense, yielding the narrow [C I] layer and hence low [C I] flux. The upper limit for NGC 6052 ($L_{[\text{C I}]}(1-0)/L_{\text{CO}(4-3)} < 0.07$) suggests a dense PDR ($n_{\text{H}} > 10^5 \text{ (cm}^{-3}\text{)}$), which is denser than those seen in the comparison galaxies (e.g., Bothwell et al. 2017; Valentino et al. 2018, 2020).

A possible explanation of high densities is compression of the ISM by the ongoing merger because the region associated with the CO (4–3) emission corresponds to the collision front based on the merger model calculation (Taniguchi & Noguchi 1991). Furthermore, the plane-parallel model might be suitable for young off-nuclear starburst regions that have not had time to erode the medium. The age of the stellar population at the CO-detected region is estimated to be ~ 5.5 Myr by modeling of the mid-infrared atomic lines (Whelan et al. 2007), suggesting the presence of young off-nuclear starbursts triggered by the ongoing merger. The dense PDR regions associated with young off-nuclear starburst activities might be a hint to understand the [C I]-poor, CO-rich region in NGC 6052.

The PDRT calculations suggest that the small $L_{[\text{C I}]}(1-0)/L_{\text{TIR}}$ is indicative of a high U_{uv} . However, it is not possible to obtain U_{uv} from the $L_{[\text{C I}]}(1-0)/L_{\text{TIR}}$ obtained from our observations. This is because the ratio of the total infrared luminosity (TIR) in the observable region of the Morita Array to the galaxy-integrated total TIR luminosity (determined by IRAS measurement) is unknown. Instead, we can access the galaxy-integrated value of $([\text{O I}]_{63} + [\text{C II}]_{158})/\text{TIR}^{13}$ that can also

¹² <http://dustem.astro.umd.edu/pdrt/>

¹³ The flux of [O I]₆₃ and [C II]₁₅₈ is 82 and 138 (W m⁻¹) (Díaz-Santos et al. 2017) and the TIR flux density of 6.5×10^{-13} (W m⁻¹) is calculated from the IRAS flux density measured by Sanders et al. (2003).

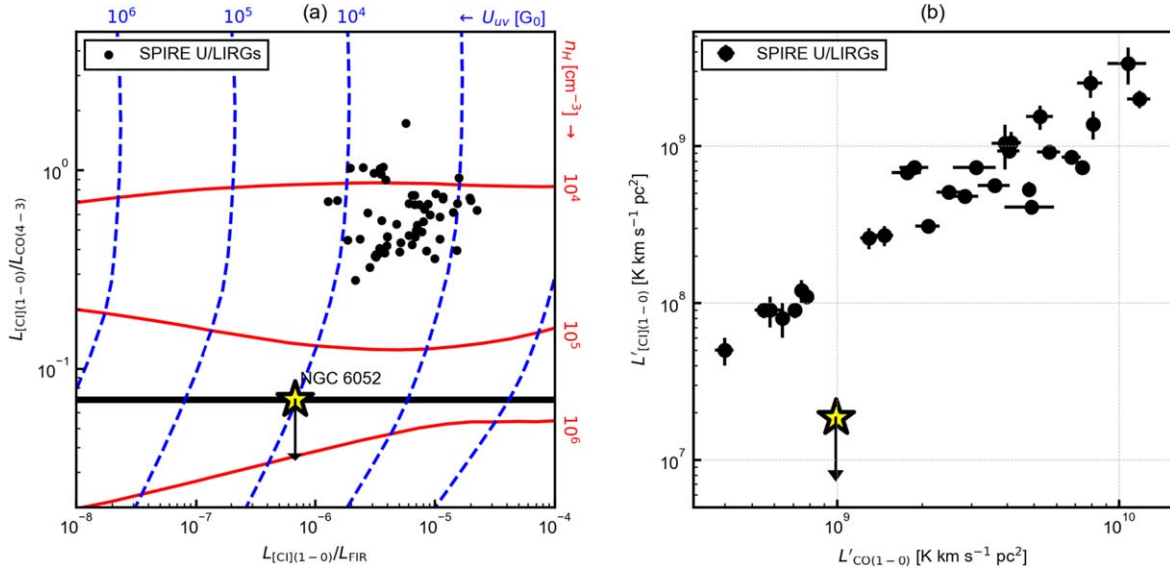


Figure 3. (a) $L_{[C I](1-0)}/L_{CO(4-3)}$ vs. $L_{[C I](1-0)}/L_{FIR}$ for PDRT calculations and observations. The red solid and blue dashed lines indicate the theoretical tracks for constant n_H (cm^{-3}) and U_{uv} [G_0], respectively. The black points indicate the nearby U/LIRG sample detected by SPIRE/FTS (Kamenetzky et al. 2016). The yellow star shows the [C I] (1–0) upper limit of NGC 6052 presented in this project. $L_{[C I](1-0)}/L_{TIR}$ is calculated without any aperture correction, indicating that this figure does not constrain the $U_{u,v}$. (b) [C I] (1–0) line luminosity vs. CO (1–0) line luminosity for U/LIRG galaxies. The symbols are the same comparison sample as (a). We note that CO (1–0) luminosity is obtained by single dish, but the upper limit of [C I] (1–0) luminosity is obtained by array observation (the missing flux is not corrected).

characterize the PDR. The ratio suggests $U_{uv} = 4-5$. (Díaz-Santos et al. 2017).

4.2. Molecular Gas Mass

In this section, we investigate whether [C I] (1–0) can trace molecular gas mass inferred from previous CO (1–0) measurements. Albrecht et al. (2007) reported the CO (1–0) integrated intensity of 82 K km s^{-1} within the $24''$ single-dish beam. The expected molecular mass is $M_{H_2}^{CO} = 8 \times 10^8 M_\odot$ assuming a CO (1–0) to H_2 conversion factor $\alpha_{CO} = 0.8 M_\odot (\text{K km s}^{-1} \text{ pc}^2)^{-1}$ (where $M_{H_2}^{line} = \alpha_{line} L'_{line}$), one of the smallest values usually considered and often applied to ULIRGs (Bolatto et al. 2013). Using the upper limit of the [C I] (1–0) luminosity, we can estimate an upper limit to the implied molecular mass through the use of $\alpha_{[C I]} = 7.3 M_\odot (\text{K km s}^{-1} \text{ pc}^2)^{-1}$ (Crocker et al. 2019). The upper limit of molecular gas mass based on [C I] is then $M_{H_2}^{[C I]} < 10^8 (M_\odot)$. This suggests that the [C I] (1–0)/CO (1–0) ratio as well as the [C I] (1–0)/CO (4–3) ratio is low. Figure 3(b) shows the relation between CO (1–0) and [C I] (1–0) luminosities for other nearby galaxies taken from Kamenetzky et al. (2016). The upper limit we measure for the [C I] (1–0)/CO (1–0) ratio in NGC 6052 is located an order of magnitude below the global relation obtained in previous surveys (e.g., Jiao et al. 2017, 2019). This suggests that [C I] (1–0) may not be a reliable tracer of molecular gas mass in NGC 6052. Although both $\alpha_{[C I]}$ and α_{CO} depend on metallicity, such a [C I]-poor region cannot be explained under the assumption of any metallicity (e.g., Bolatto et al. 2013; Glover & Clark 2016; Heintz & Watson 2020). For example, at lower metallicities CO is would be more easily dissociated due to the lack of dust shielding, and consequently more carbon would be observed as [C I].

An alternative explanation for the big difference between NGC 6052 and other systems in Figure 3 is resolving out spatially extended diffuse gas emission. The emission from [C I] (1–0) and CO (1–0) are usually co-extensive, and both are

likely to originate predominantly from extended, low excitation gas. On the other hand, higher- J CO emission is likely dominated by compact, high excitation gas and the contribution from more diffuse gas. Thus, the [C I] (1–0)/CO (4–3) and [C I] (1–0)/CO (1–0) ratios may represent properties of very different phases of the gas, and it is possible that the Morita Array resolved out most extended emission from [C I] (1–0). In such a case, the large difference seen in Figure 3(b) can be explained if $>88\%$ of the flux of [C I] (1–0) was missing due to its extended structure, possibly larger than the Maximum Recoverable Scale of ~ 4.3 kpc. While such large missing flux is not generally seen in other galaxies, follow-up mosaic mapping observations including 12 m, Morita Array, and total power would be important to check the possibility of an extremely extended [C I] (1–0) distribution in NGC 6052. In either case, whether [C I]-poor or with an extremely extended [C I] distribution, NGC 6052 is a unique laboratory to investigate how the merger process impacts the use of [C I] as a mass tracer.

5. Summary

We report [C I] (1–0) and CO (4–3) observations of the nearby merging galaxy NGC 6052 using the ALMA Morita Array. We detect CO (4–3) with high significance (signal-to-noise ratio of >40), but [C I] (1–0) is undetected to a stringent upper limit of 0.07 times the strength of the CO (4–3) emission. Models of PDRs can explain the weakness of [C I] as the result of gas densities that are unusually high ($n_H > 10^5 \text{ cm}^{-3}$), which might arise naturally in the collision front of the ongoing merger. In addition, [C I] (1–0) is far weaker than expected for the amount of molecular gas inferred from the existing measurements of CO (1–0) and CO (2–1) in NGC 6052. This may suggest a [C I]-poor, CO-rich system and/or extremely extended diffuse molecular gas distribution that is not well documented in the literature.

This work was supported by the National Science Foundation of China (11721303, 11991052) and the National Key R&D Program of China (2016YFA0400702). We are grateful to the anonymous referee for useful comments that helped the authors to improve the Letter. The authors appreciate Prof. Masami Ouchi (The University of Tokyo) and Prof. Takuya Hashimoto (Tsukuba University) who provided a comfortable and fruitful research environment during the COVID-19 pandemic time. This Letter makes use of the following ALMA data: ADS/JAO.ALMA #2018.1 00994. ALMA is a partnership of ESO (representing its member states), NSF (USA) and NINS (Japan), together with NRC (Canada), MOST and ASIAA (Taiwan), and KASI (Republic of Korea), in cooperation with the Republic of Chile. The Joint ALMA Observatory is operated by ESO, AUI/NRAO and NAOJ. T.S. acknowledges funding from the European Research Council (ERC) under the European Union’s Horizon 2020 research and innovation programme (grant agreement No. 694343). D.I. is supported by JSPS KAKENHI grant No. 15H02074 and 18H03725.

Appendix Notes about SPIRE/FTS Measurements

NGC 6052 was observed by SPIRE/FTS (Kamenetzky et al. 2016; Lu et al. 2017). We downloaded the science data products automatically generated by the data processing pipelines from “Herschel science archive.”¹⁴ Same as Lu et al. (2017), we adopt point-source calibration and fit simultaneously the continuum and emission lines using a fifth-order polynomial and sinc profiles following the “Spectrometer Line Fitting” script in

Herschel Interactive Data Processing Environment (HIPE). Figure A1 shows the continuum-subtracted SPIRE/FTS spectrum (black solid lines) and the fitting results (green dashed lines). Only CO (4–3) is marginally detected with the signal-to-noise ratio (S/N) of 3.9 and both [C I] (1–0) and [C I] (2–1) are not detected ($S/N \lesssim 3$). In our analysis, S/N is calculated using the ratio between peak flux density obtained by spectrum fitting and the rms value of the flux density in the line-free frequency range (i.e., 460–480 GHz for CO(4–3) and [C I] (1–0) and 800–820 GHz for [C I] (2–1) emissions), which is not the same method in Kamenetzky et al. (2016) and Lu et al. (2017). Since the S/N is ~ 3 for [C I] (1–0) and [C I] (2–1), these lines may be considered as “detection” in different methods. For example, [C I] (1–0) emission line is considered as “detection” in the analysis by Kamenetzky et al. (2016), but “nondetection” by Lu et al. (2017) and our analysis. In Table A1, the velocity-integrated flux (and 3σ upper limits) measured by our analysis, Kamenetzky et al. (2016), and Lu et al. (2017) are shown. Comparison of these SPIRE measurements with our Morita Array result implies that the CO (4–3) flux recovered by the Morita Array may be $\sim 30\%$ of the total. But, given the fact that the Herschel beam is four times the solid angle of our FoV and the considerable uncertainties in the FTS measurement (i.e., the intensity is an analytical solution assuming sinc function for the spectroscopically unresolved line¹⁵), it is impossible to directly compare SPIRE flux and our Morita Array’s results. Further discussion of SPIRE/FTS measurements is beyond the aim of this Letter because the line detection is marginal even for the CO (4–3) emission.

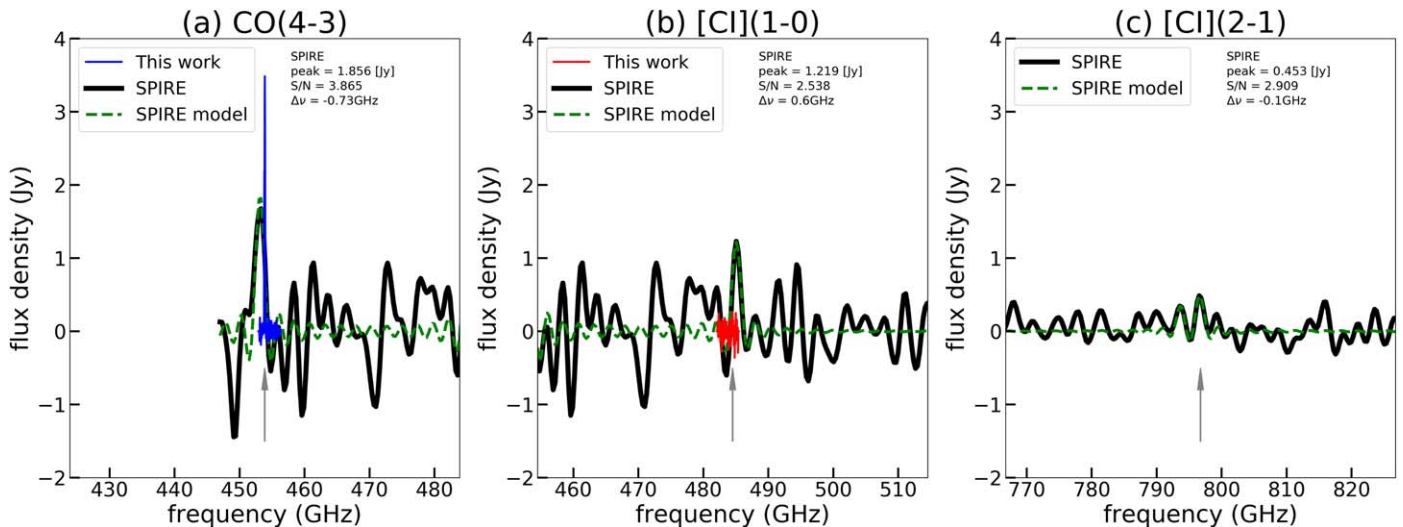


Figure A1. (a)–(c) The black line indicates the continuum-subtracted SPIRE/FTS spectrum around CO (4–3), [C I] (1–0), and [C I] (2–1) emission. The best fit is shown as a green dashed line. The peak flux density and the frequency offsets from the systematic velocity measured by CO (4–3) are shown at the upper right corners for each panel. The S/N is calculated by our own definition (see the Appendix text). Supplementary, the CO (4–3) (blue) and [C I] (1–0) (red) spectra obtained by this project are shown in (a) and (b), respectively. The gray arrows indicate the frequencies of CO (4–3) and [C I] (1–0), and [C I] (2–1) corresponding to the systemic velocity. The second peak fitted in (c) is for the CO (7–6) emission line.

¹⁴ <http://archives.esac.esa.int/hsa/whsa/>












¹⁵ http://herchel.esac.esa.int/hcss-doc-15.0/load/spire_drg/html/spire_spec_analysis.html

Table A1
SPIRE/FTS Summary for NGC 6052

Line	$S_{\text{line}} dv$ (Jy km s ⁻¹) Our Analysis	$S_{\text{line}} dv$ (Jy km s ⁻¹) Kamenetzky et al. (2016)	$S_{\text{line}} dv$ (Jy km s ⁻¹) Lu et al. (2017)
(1)	(2)	(3)	(4)
CO(4–3)	1451 ± 128	1400 ⁺⁵⁰⁰ ₋₄₀₀	1600 ± 300
[C I] (1–0)	<1055	940 ⁺³⁰⁰ ₋₃₁₀	<1058
[C I] (2–1)	<208	160 ⁺⁶⁰ ₋₇₂	210 ± 30

Note. (1) Line name. (2)–(4) The velocity-integrated line flux measured by this project, Kamenetzky et al. (2016), and Lu et al. (2017).

ORCID iDs

Tomonari Michiyama  <https://orcid.org/0000-0003-2475-7983>
 Junko Ueda  <https://orcid.org/0000-0003-3652-495X>
 Ken-ichi Tadaki  <https://orcid.org/0000-0001-9728-8909>
 Alberto Bolatto  <https://orcid.org/0000-0002-5480-5686>
 Toshiaki Saito  <https://orcid.org/0000-0002-2501-9328>
 Takuji Yamashita  <https://orcid.org/0000-0002-4999-9965>
 Ming-Yang Zhuang  <https://orcid.org/0000-0001-5105-2837>
 Kouichiro Nakanishi  <https://orcid.org/0000-0002-6939-0372>
 Daisuke Iono  <https://orcid.org/0000-0002-2364-0823>
 Ran Wang  <https://orcid.org/0000-0003-4956-5742>
 Luis C. Ho  <https://orcid.org/0000-0001-6947-5846>

References

- Albrecht, M., Krügel, E., & Chini, R. 2007, *A&A*, 462, 575
 Bisbas, T. G., Papadopoulos, P. P., & Viti, S. 2015, *ApJ*, 803, 37
 Bolatto, A. D., Wolfire, M., & Leroy, A. K. 2013, *ARA&A*, 51, 207
 Bothwell, M. S., Aguirre, J. E., Aravena, M., et al. 2017, *MNRAS*, 466, 2825
 Burton, M. G., Ashley, M. C. B., Braiding, C., et al. 2015, *ApJ*, 811, 13
 Cicone, C., Severgnini, P., Papadopoulos, P. P., et al. 2018, *ApJ*, 863, 143
 Crocker, A. F., Pellegrini, E., Smith, J.-D. T., et al. 2019, *ApJ*, 887, 105
 Díaz-Santos, T., Armus, L., Charmandaris, V., et al. 2017, *ApJ*, 846, 32
 Glover, S. C. O., & Clark, P. C. 2016, *MNRAS*, 456, 3596
 Habing, H. J. 1968, *BAN*, 19, 421
 Hainline, L. J., Scoville, N. Z., Yun, M. S., et al. 2004, *ApJ*, 609, 61
 Heintz, K. E., & Watson, D. 2020, *ApJL*, 889, L7
 Ikeda, M., Oka, T., Tatematsu, K., et al. 2002, *ApJS*, 139, 467
 Israel, F. P., & Baas, F. 2002, *A&A*, 383, 82
 Israel, F. P., Rosenberg, M. J. F., & van der Werf, P. 2015, *A&A*, 578, A95
 Izumi, T., Nguyen, D. D., Imanishi, M., et al. 2020, arXiv:2006.09406
 James, A., Dunne, L., Eales, S., et al. 2002, *MNRAS*, 335, 753
 Jiao, Q., Zhao, Y., Lu, N., et al. 2019, *ApJ*, 880, 133
 Jiao, Q., Zhao, Y., Zhu, M., et al. 2017, *ApJL*, 840, L18
 Kamenetzky, J., Rangwala, N., Glenn, J., et al. 2016, *ApJ*, 829, 93
 Kaufman, M. J., Wolfire, M. G., & Hollenbach, D. J. 2006, *ApJ*, 644, 283
 Kaufman, M. J., Wolfire, M. G., Hollenbach, D. J., et al. 1999, *ApJ*, 527, 795
 Kramer, C., Cubick, M., Röllig, M., et al. 2008, *A&A*, 477, 547
 Krips, M., Martín, S., Sakamoto, K., et al. 2016, *A&A*, 592, L3
 Lu, N., Zhao, Y., Díaz-Santos, T., et al. 2017, *ApJS*, 230, 1
 McMullin, J. P., Waters, B., Schiebel, D., et al. 2007, in ASP Conf. Ser. 376, *Astronomical Data Analysis Software and Systems XVI*, ed. R. A. Shaw, F. Hill, & D. J. Bell (San Francisco, CA: ASP), 127
 Miyamoto, Y., Seta, M., Nakai, N., et al. 2018, *PASJ*, 70, L1
 Mo, H., van den Bosch, F. C., & White, S. 2010, *Galaxy Formation and Evolution* (Cambridge: Cambridge Univ. Press)
 Ojha, R., Stark, A. A., Hsieh, H. H., et al. 2001, *ApJ*, 548, 253
 Oka, T., Yamamoto, S., Iwata, M., et al. 2001, *ApJ*, 558, 176
 Papadopoulos, P. P., Bisbas, T. G., & Zhang, Z.-Y. 2018, *MNRAS*, 478, 1716
 Papadopoulos, P. P., & Greve, T. R. 2004, *ApJL*, 615, L29
 Papadopoulos, P. P., Thi, W.-F., & Viti, S. 2004, *MNRAS*, 351, 147
 Planck Collaboration, Ade, P. A. R., Aghanim, N., et al. 2016, *A&A*, 594, A13
 Pound, M. W., & Wolfire, M. G. 2008, in ASP Conf. Ser. 394, *Astronomical Data Analysis Software and Systems*, ed. R. W. Argyle, P. S. Bunclark, & J. R. Lewis (San Francisco, CA: ASP), 654
 Rupke, D. S. N., Veilleux, S., & Baker, A. J. 2008, *ApJ*, 674, 172
 Sage, L.-J., Loose, H.-H., & Salzer, J. J. 1993, *A&A*, 273, 6
 Salak, D., Nakai, N., Seta, M., et al. 2019, *ApJ*, 887, 143
 Sanders, D. B., Mazzarella, J. M., Kim, D.-C., et al. 2003, *AJ*, 126, 1607
 Shi, F., Kong, X., Li, C., et al. 2005, *A&A*, 437, 849
 Shimajiri, Y., Sakai, T., Tsukagoshi, T., et al. 2013, *ApJL*, 774, L20
 Solomon, P. M., & Vanden Bout, P. A. 2005, *ARA&A*, 43, 677
 Tadaki, K., Iono, D., Yun, M. S., et al. 2018, *Natur*, 560, 613
 Taniguchi, Y., & Noguchi, M. 1991, *AJ*, 101, 1601
 Tielens, A. G. G. M., & Hollenbach, D. 1985, *ApJ*, 291, 722
 Ueda, J., Iono, D., Yun, M. S., et al. 2014, *ApJS*, 214, 1
 Valentino, F., Magdis, G. E., Daddi, E., et al. 2018, *ApJ*, 869, 27
 Valentino, F., Magdis, G. E., Daddi, E., et al. 2020, *ApJ*, 890, 24
 Walter, F., Weiß, A., Downes, D., et al. 2011, *ApJ*, 730, 18
 Whelan, D. G., Devost, D., Charmandaris, V., et al. 2007, *ApJ*, 666, 896